Computerized Medical Imaging and Graphics 108 (2023) 102256

Contents lists available at ScienceDirect

Computerized Medical Imaging and Graphics

journal homepage: www.elsevier.com/locate/compmedimag

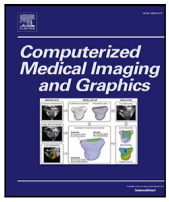

Retinal OCT speckle as a biomarker for glaucoma diagnosis and staging

Pedro G. Vaz [a,*], Luisa Sanchez Brea [b,c], Vania Bastos Silva [a,b], Jan van Eijgen [d,e], Ingeborg Stalmans [d,e], João Cardoso [a], Theo van Walsum [b], Stefan Klein [b], João Barbosa Breda [d,f,g], Danilo Andrade De Jesus [b,c]

[a] LIBPhys, Department of Physics, University of Coimbra, Coimbra, Portugal
[b] Department of Radiology and Nuclear Medicine, Erasmus MC, Rotterdam, The Netherlands
[c] Department of Ophthalmology, Erasmus MC, Rotterdam, The Netherlands
[d] Department of Neurosciences, KU Leuven, Leuven, Belgium
[e] Department of Ophthalmology, University Hospitals UZ Leuven, Leuven, Belgium
[f] Cardiovascular R&D Center, Faculty of Medicine of the University of Porto, Porto, Portugal
[g] Department of Ophthalmology, São João Universitary Hospital Center, Porto, Portugal

ARTICLE INFO

Keywords:
OCT
Speckle
Glaucoma
Staging

ABSTRACT

This paper presents a novel image analysis strategy that increases the potential of macular Optical Coherence Tomography (OCT) by using speckle features as biomarkers in different stages of glaucoma.

A large pool of features (480) were computed for a subset of macular OCT volumes of the Leuven eye study cohort. The dataset contained 258 subjects that were divided into four groups based on their glaucoma severity: Healthy (56), Mild (94), Moderate (48), and Severe (60). The OCT speckle features were categorized as statistical properties, statistical distributions, contrast, spatial gray-level dependence matrices, and frequency domain features. The averaged thicknesses of ten retinal layers were also collected. Kruskal–Wallis H test and multivariable regression models were used to infer the most significant features related to glaucoma severity classification and to the correlation with visual field mean deviation.

Four features were selected as being the most relevant: the ganglion cell layer (GCL) and the inner plexiform layer (IPL) thicknesses, and two OCT speckle features, the data skewness computed on the retinal nerve fiber layer (RNFL) and the scale parameter (a) of the generalized gamma distribution fitted to the GCL data. Based on a significance level of 0.05, the regression models revealed that RNFL skewness exhibited the highest significance among the features considered for glaucoma severity staging (p-values of 8.6×10^{-6} for the logistic model and 2.8×10^{-7} for the linear model). Furthermore, it demonstrated a strong negative correlation with the visual field mean deviation ($\rho = -0.64$). The *post hoc* analysis revealed that, when distinguishing healthy controls from glaucoma subjects, GCL thickness is the most relevant feature (p-value of 8.7×10^{-5}). Conversely, when comparing the Mild versus Moderate stages of glaucoma, RNFL skewness emerged as the only feature exhibiting statistical significance (p-value = 0.001).

This work shows that macular OCT speckle contains information that is currently not used in clinical practice, and not only complements structural measurements (thickness) but also has a potential for glaucoma staging.

1. Introduction

Glaucoma is the leading cause of irreversible blindness, affecting over 80 million people worldwide (Tham et al., 2014). Since the disease is correlated with ageing, these numbers are expected to greatly increase in coming decades. Glaucoma is a chronic progressive optic neuropathy characterized by the thinning of the retinal nerve fiber layer (RNFL) and the cupping of the optic disc, both happening as a result of axonal and retinal ganglion cell loss (Weinreb et al., 2014) and leading to corresponding visual field defects. Glaucoma screening, diagnosis, and severity classification are based on the clinical analysis of intraocular pressure (IOP) measurements, visual field (VF), and structural optic disc assessment (e.g. using optical coherence tomography (OCT)) (Jesus et al., 2019). The recent developments in image enhancement and automatic segmentation in OCT imaging have

* Corresponding author.
E-mail address: pvaz@uc.pt (P.G. Vaz).

https://doi.org/10.1016/j.compmedimag.2023.102256
Received 9 February 2023; Received in revised form 23 May 2023; Accepted 30 May 2023
Available online 8 June 2023

enabled the determination of several biomarkers for clinical applications. Most of the biomarkers are related to morphological analysis of either the macula or the optic disc (e.g. RNFL thickness Bowd et al., 2000, neuroretinal rim area, optic disc area, and Bruch's membrane opening Gmeiner et al., 2016; Mohammadzadeh et al., 2020). The structural changes assessed by these biomarkers are especially important for early stages of glaucoma, as they can happen before any functional damage is visible (Kuang et al., 2015). However, when the disease has progressed to an advanced stage, most biomarkers reach a point where further functional decline does not cause any alterations in the structural exams, and cannot be identified in OCT scans (Bowd et al., 2017).

Despite the different tools available in clinical practice, there is no gold standard biomarker for the diagnosis of glaucoma (Kostianeva-Zhelinska et al., 2018), which often leads to several follow up appointments before a diagnosis can be achieved and some misclassified cases (Butt et al., 2016). Henceforth, disease progression is assessed by OCT and/or optic disc visual inspection (e.g. fundus imaging) as well as by visual field metrics (such as mean deviation (VF MD)), since visual field defects increase with disease severity (Wu et al., 2022). However, VF MD measurements require considerable concentration and cooperation from the patient, which may lead to low repeatability and reproducibility for some cases (Patel et al., 2015). Thus, new quantitative and reproducible biomarkers are essential to improve glaucoma diagnosis, ideally at earlier stages, and assess its progression ideally until later stages. It is in these more severe cases when visual fields are usually less reliable and OCT metrics have reached the limit of their discriminating ability, usually mentioned as "floor effect" (Bowd et al., 2017).

As a way to provide new insights and improve glaucoma progression assessment, researchers have introduced new biomarkers that go beyond the morphological analysis of OCT images such as speckle-based features (Gary et al., 2021; Silva et al., 2022). In OCT imaging, the incident light travels through different optical paths until it reaches the image plane. Apart from reflection and scattering, the light intensity at each point of the plane results from interference of all light waves at that single point creating granular patterns, known as speckles (Kirillin et al., 2014; Vaz et al., 2017). Since these patterns are influenced by tissue properties (e.g. local scattering and particle motion), their analysis results in sub-resolution and structural information (De Pretto et al., 2015). Features based on OCT speckle are still in early stages of adoption, in spite of having provided good results in simulation models or preclinical OCT data (Danielewska et al., 2021; Silva et al., 2022). Experimental uses of OCT speckle features *in-vivo* have also been documented (Jesus and Iskander, 2015; Demidov et al., 2019). For instance, the statistical modulation of the corneal OCT speckle intensity was performed in order to understand its relation with IOP (Niemczyk et al., 2021; Jesus et al., 2017) and to differentiate between glaucoma suspects, patients, and healthy controls (Iskander et al., 2020). These studies have shown that OCT speckle statistics can be used not only for identifying IOP-induced changes in the optical scattering within the corneal stroma, but also in corneal geometry. Another study (Demidov et al., 2019) focused on the analysis of spatial speckle statistics to retrieve information from low-scattering biological structures, specifically lymphatic vessels and nerves. However, to the best of our knowledge, none of the studies presented so far has retrieved speckle-based information from the retinal layers and inferred its potential for assisting the diagnosis and staging.

The goal of this study is to explore whether the analysis of OCT speckle from retinal layers can be used to assist in glaucoma diagnosis and severity classification. For that, a broad group of OCT speckle features (470) from macula-centred volumes of healthy controls and glaucoma subjects have been retrieved and studied. Moreover, these features were compared with structural features (retinal layers' thickness) to determine which features are better to discriminate early disease stages and perform patient staging.

2. Methods

2.1. Dataset

The dataset used in this work is a subset of the Leuven Eye Study (LES) cohort (Abegão Pinto et al., 2016). The LES is one of the largest clinical trials on glaucoma, and it includes healthy controls, glaucoma suspects, and normal tension glaucoma (NTG), primary open angle glaucoma (POAG), and ocular hypertension (OHT) patients. In this study, the macular OCT data of 258 subjects and a subset of clinical metadata (age, sex, IOP, and VF MD) were used.

The glaucoma patients were clustered into three severity groups, according to the European Glaucoma Society guidelines (Society, 2021). Patients with VF MD higher or equal to −6 dB were considered to have Mild glaucoma, between −6 dB and −12 dB were considered to have Moderate glaucoma, and those with VF MD lower than −12 dB were classified as severe cases. Table 1 summarizes the data demographics, including the mean values for VF MD and IOP. It is important to notice that IOP is lower than expected in Moderate and Severe cases due to the topical medication administered to advanced glaucoma patients (Armstrong et al., 2017).

The OCT device used for the acquisition was the Cirrus 4000 HD OCT (Carl Zeiss, Dublin, CA), with an axial and lateral resolution of 5 and 15 μm, respectively. Each OCT volume had 128 B-scans, with 1024 × 512 pixels each. All pixel intensities were stored in 8-bits. Prior to the data analysis, an inverse logarithmic transform and normalization between 0 and 1 ($y = 10^{x/255-1}$) were applied to all OCT volumes.

Since age and sex are known confounders in glaucoma (Guedes et al., 2011), the univariate Kruskal–Wallis H test (age) and the Chi-square test of independence (sex) were used for assessing possible differences in these variables between severity groups.

2.2. Image segmentation

Ten retinal layers were segmented for each B-scan. The segmentation was performed with the multi-surface segmentation Iowa Reference Algorithm (Retinal Image Analysis Lab, Iowa Institute for Biomedical Imaging, Iowa City, IA) (Abràmoff et al., 2010). The segmented layers, from top to bottom, were: retinal nerve fiber layer (RNFL); ganglion cell layer (GCL); inner plexiform layer (IPL); inner nuclear layer (INL); outer plexiform layer (OPL); outer nuclear layer (ONL); inner photoreceptor segment (IS); inner-segment/outer-segment (IS/OS) junction; outer photoreceptor segment (OS); and retinal pigment epithelium (RPE). Fig. 1 shows an example of a B-scan and the respective segmentation.

2.3. Features computation

The speckle-based features (47) and the averaged thickness (1) were computed for each of the 10 segmented layers. The code used to determine these values can be found in Repository (2023).

2.3.1. Speckle features

The speckle features were divided in 5 different groups: statistical properties, statistical distributions, contrast, spatial grey-level dependence matrices (SGLDM), and Fourier domain analysis (Silva et al., 2022). The computed features are summarized in Table 2 and in the following subsections.

i. Statistical properties

Statistical properties of OCT pixel intensity have been used to infer speckle characteristics in previous studies (Roy et al., 2015). These properties include: mean, standard deviation, kurtosis, and skewness of the pixels' intensities.

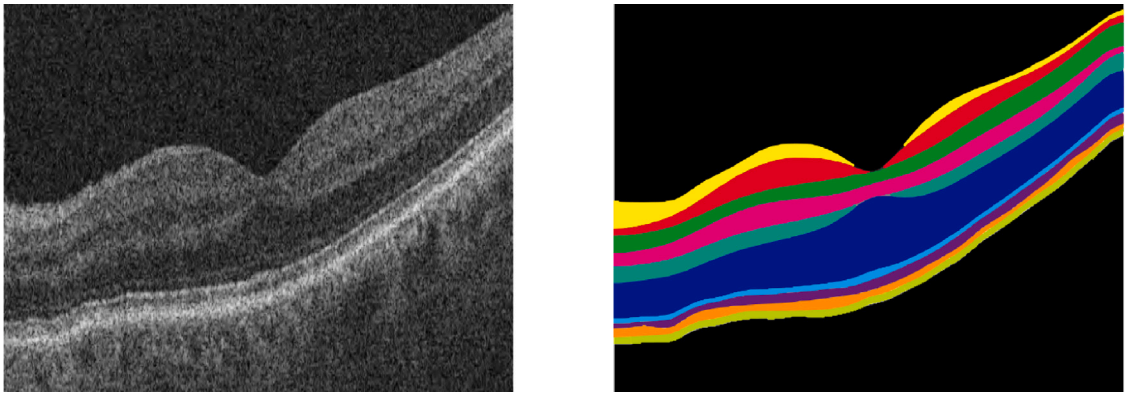

Fig. 1. OCT B-scan centred at the macula (left) and the respective segmentation mask using the Iowa Reference Algorithm (Abràmoff et al., 2010) (right). The segmented layers, from the top to the bottom, are: RNFL (yellow), GCL (red), IPL (green), INL (magenta), OPL (teal), ONL (blue), IS (cyan), IS/OS (purple), OS (orange), and RPE (lime).

Table 1
Demographics, VF MD, and IOP for each group (n = number of subjects; M/F = male/female; OS/OD = left/right eye).

Group	n	Sex (M/F)	Eye (OS/OD)	Age (years)	VF MD (dB)	IOP (mm Hg)
Healthy	56	32/24	27/29	62.9 ± 12.3	–	15.1 ± 3.1
Mild	94	45/49	42/52	67.5 ± 10.3	−1.8 ± 2.3	14.0 ± 4.5
Moderate	48	27/21	19/29	65.4 ± 8.5	−8.5 ± 1.7	12.7 ± 4.1
Severe	60	35/25	32/28	68.8 ± 11.3	−18.1 ± 4.4	12.4 ± 4.4
TOTAL	258	139/120	121/138	66.4 ± 10.9	−6.4 ± 7.6	13.6 ± 4.3

Table 2
Summary of the speckle features that were calculated from each retinal layer.

Group	Speckle features	N. of features
Statistical properties	Mean	1
	Standard deviation	1
	Skewness	1
	Kurtosis	1
Statistical distributions	Rayleigh (a)	1
	K (ν, ϕ, L)	3
	Gamma (a, d)	2
	Generalized gamma (a, d, p)	3
	Weibull (a, d)	2
	Nakagami (d, Ω)	2
	Rician (a, ν)	2
	Lognormal (μ, σ)	2
Contrast	Mean	1
	Standard deviation	1
SGLDM	Energy	4
	Entropy	4
	Correlation	4
	Local homogeneity	4
	Contrast	4
Fourier Domain	Relative power	4
Total		47

ii. Statistical distributions

Several statistical distributions (probability density functions, PDFs) have been used to model OCT speckle in previous works (Silva et al., 2022). The parameters describing these distributions change according to the tissue properties, specifically the dimension and arrangement of the scatterers in the sample (Jesus and Iskander, 2017). For each layer, the OCT pixel intensity values were fitted to eight different PDFs, each one with a specific set of parameters ranging from one (Rayleigh) to three (Generalized Gamma and K). A full mathematical description of these PDFs can be found in Silva et al. (2022) while their equations are presented in Appendix A.

iii. Contrast

The OCT volumetric contrast map was determined using a local approach similar to the one used for laser speckle contrast imaging in Vaz et al. (2016). The contrast value was defined as the ratio between the signal's standard deviation (σ) to its mean (μ) (Eq. (A.9)). The contrast values were determined in windows of 3 × 3 × 3 voxels over the entire OCT volume using one pixel stride. After the contrast maps were computed, the mean and standard deviation of the voxels corresponding to each segmented layer were calculated and used as features.

iv. Spatial gray-level dependence matrices

Spatial gray-level dependence matrices (SGLDM) have also been used for texture analysis in OCT speckle images (Kasaragod et al., 2010). SGLDM measure variations in the brightness of an image, and are determined by the estimation of the second-order joint-probability distribution of each combination of grey-level values that occur next to each other (distance equals one pixel), averaged over directions of 0°, 45°, 90° and 135°. Assuming the images are normalized and quantified with L grey scale values, each $f(i, j \mid d, \theta)$ is the probability of a pixel with value i being at a distance d from a pixel with gray value of j in the θ direction. An $L \times L$ matrix can be created for a chosen direction θ and distance d.

Several features were extracted from these matrices, namely the energy (Eq. (A.10)), entropy (Eq. (A.11)), correlation (Eq. (A.12)), local homogeneity (Eq. (A.13)), and contrast (Eq. (A.14)) (Hilal et al., 2022).

The computation of these 5 features for each SGLDM (4 directions) resulted in 20 features per retinal layer. Since the calculation of a SGLDM requires an image as input, instead of a volume, each B-scan was analyzed individually (Kasaragod et al., 2010). Then, the mean of each feature was calculated for all the B-scans in a volume.

v. Frequency domain

A frequency domain analysis of each OCT volume was performed using a 3D discrete Fourier transform (DFT). The Fourier space was further divided in four concentric regions (low, mid-low, mid-high,

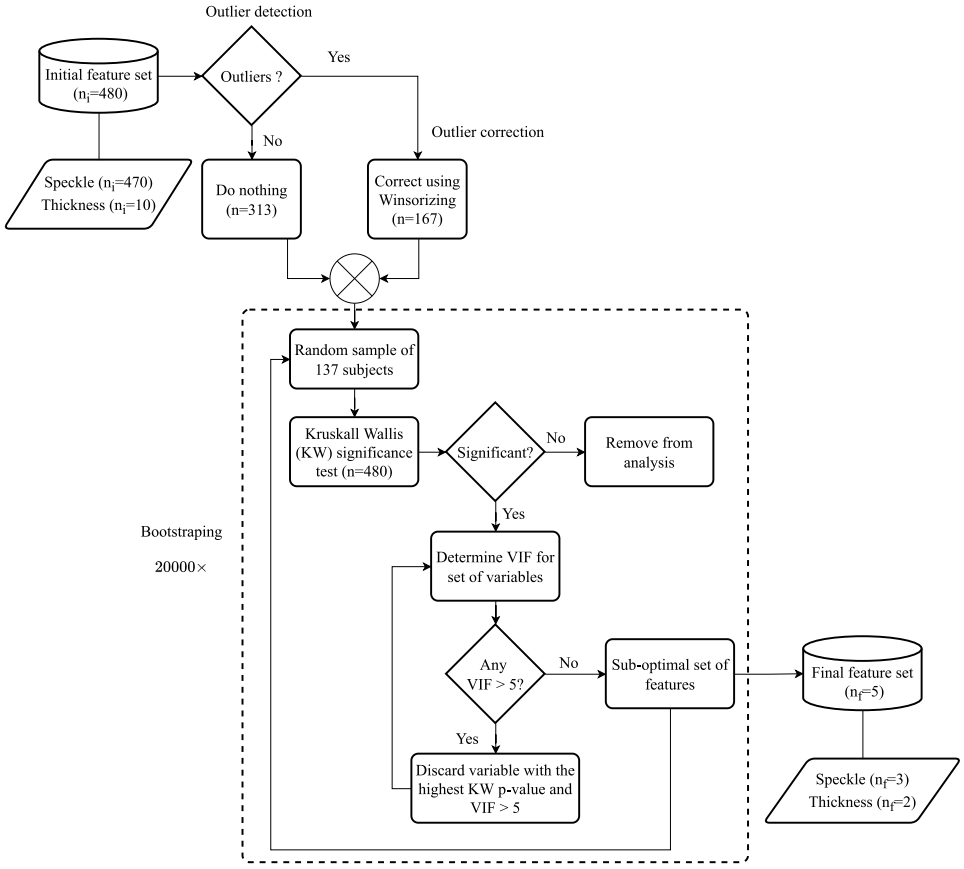

Fig. 2. Flowchart of the pre-processing steps and bootstrap feature selection method.

and high frequency). The integral of the spectral amplitude of each region was divided by the total spectral amplitude of the Fourier space resulting in 4 features for each tissue layer.

2.3.2. Thickness features

The thickness of each of the 10 layers was calculated by averaging the thickness of all A-scans in the respective volume. This resulted in 10 measurements (thickness-based features) per subject.

2.4. Outlier correction

In this study, any value that was greater than five standard deviations from the mean value was considered an outlier. These features were corrected using the Winsorizing method (Ghosh and Vogt, 2012). In practice, the method corrects low or high outliers by adjusting the value to the 5th or the 95th data percentile, respectively.

2.5. Statistical analysis

Since the data did not follow a normal distribution, the non-parametric univariate Kruskal–Wallis H test was used to determine which of the 480 features presented statistically significant differences between Healthy, Mild, Moderate and Severe subjects. A Bonferroni correction was applied due to the large number of variables analyzed. The features that presented a $p < 0.05/480 = 1.04 \times 10^{-4}$ were considered as candidates for glaucoma staging.

Hereafter, the variance inflation factor (VIF) (Kim, 2019) was used to remove variables with large values of multicollinearity using an iterative process. First, a multivariable linear regression model was fitted for each variable against the other variables that meet the Kruskall–Wallis H test criterion. Then, the VIF was determined for each variable using the equation (Kim, 2019):

$$\mathrm{VIF}_i = \frac{1}{1 - R_i^2} \tag{1}$$

where R_i^2 is the coefficient of determination of the linear regression when considering feature i as the dependent variable. From the set of variables with VIF ≥ 5, the variable with the highest Kruskal–Wallis p-value was removed from the original set. The process is repeated until all the variables presented a VIF<5.

This statistical analysis was applied using a bootstrapping approach with 50% of the subjects (137) and 20 000 runs. For each run, a set of optimal features was found. The final set of features was considered to be the one that was selected the most. Fig. 2 summarizes the pre-processing steps and the bootstrap feature selection method and the next paragraph provide detail on each one of the statistical analysis steps.

2.6. Model fitting

The final set of relevant features and patients' age were fitted to two different types of models (classification and regression) following two approaches, dividing the data in four or two classes. For both, all features were standardized (transformed to have zero mean and unitary standard deviation). The groups were tested using the stratification described in Table 1 and the approaches are detailed in the following subsections.

Table 3
Set of features that presented a Kruskal–Wallis test H p-value lower than 1.04×10^{-4} and VIF < 5. The last three columns show the correlation coefficient of the univariate linear regression between the feature and the respective layer thickness, the VF MD and age. The results for age are also present for reference.

Layer	Feature	p-value	VIF	Corr. with thickness	Corr. with VF MD	Corr. with Age
RNFL	Skewness	1.1e−27	2.6	−0.27	−0.64	0.22
	Lognormal μ	4.6e−25	2.6	0.22	0.49	−0.29
GCL	Gen. Gamma a	1.7e−09	1.3	−0.48	−0.34	0.14
	Thickness	7.7e−24	2.7	1	0.57	−0.23
IPL	Thickness	1.9e−20	2.3	1	0.55	−0.16
	Age	1.5e−02	–	–	−0.16	–

Table 4
Four-class models (ordinal logit regression and multivariable linear regression) with the respective statistically significant features, coefficients and confidence intervals. Statistically significant features implicate a non-zero model coefficient with a confidence level of 95%.

Model	Layer	Feature	Coeff.	Conf. Interval 95%	p-value
Ordinal logistic regression (Glaucoma severity)	RNFL	Skewness	1.00	[0.56 1.43]	8.6e−06
	GCL	Gen. Gamma a	0.29	[0.01 0.57]	4.7e−02
	GCL	Thickness	−0.80	[−1.22 − 0.38]	1.8e−04
	IPL	Thickness	−0.41	[−0.79 − 0.03]	3.6e−02
Multivariable linear regression (VF MD)	RNFL	Skewness	−3.64	[−4.98 − 2.29]	2.8e−07
	IPL	Thickness	1.62	[0.40 2.84]	9.8e−03

i. Four-class models

An ordered logistic regression based on the 4-classes (Healthy, Mild, Moderate, and Severe) was fitted to the dataset. The order was defined from 0 (Healthy) to 3 (Severe). The odds' ratio of each variable can be obtained by exponentiation of the model coefficients. A variable was considered to be significant for the model if its coefficient was different than zero with a 95% confidence interval (Ranganathan et al., 2017). The model is defined as follows,

$$log \frac{P(S \leq j)}{P(S > j)} = \beta_{j0} + \beta_1 x_1 + \cdots + \beta_p x_p \quad (2)$$

where S stands for severity, β_p is the model coefficient for the variable number p, β_{j0} is the interception coefficient, and j is the index of the class $\in \{0, 1, 2, 3\}$.

In addition, a multivariable linear regression model was used to fit VF MD (which is the value used to categorize the severity groups) to the same set of features plus age. The Healthy group was excluded from this analysis because the VF MD is not regularly measured for healthy subjects.

ii. Two-class models

A two-class multivariable logistic regression model was fitted to pairs of groups as a *post hoc* analysis. Four different models were considered, comparing Healthy vs. Glaucoma and consecutive stages: Healthy vs. Mild, Mild vs. Moderate, and Moderate vs. Severe, in order to check the discriminant power of OCT speckle and anatomical features for each specific case. Moreover, the area under the receiver operating characteristic curve (AUC) was computed to show that they are in agreement with the values reported in literature for the LES dataset (Abegão Pinto et al., 2016).

3. Results

3.1. Outlier correction

In total, 165 features were identified as having outliers, with a maximum number of 6 outliers per feature. This corresponds to a maximum percentage of 2% (6/258) of the total number of elements.

3.2. Statistical analysis

Age and sex were analyzed to check for association with the glaucoma severity groups. No statistically significant association was found for sex (p-value = 0.5, 95% confidence interval) but it was for age (p-value = 0.015, 95% confidence interval). Consequently, age was considered as an independent variable in all models presented in this study.

From the original 480 set of features (470 speckle + 10 layer thicknesses), only 5 (3 speckle and 2 thickness features) were considered statistically relevant for the analysis of glaucoma. This set of features was selected 510 times with the bootstrap method. All the features on this set presented a p-value lower than 1.04×10^{-4} for the comparison between severity groups and, at the same time, comprise a set where all the features have a VIF < 5. Table 3 summarizes the results obtained for the Kruskal–Wallis H test p-values and presents the univariate correlation of each feature with the VF MD, thickness of the respective layer, and age. The lowest p-value (1.1×10^{-27}) was obtained for RNFL skewness, followed closely by RNFL Lognormal μ (4.6×10^{-25}) and GCL thickness (7.7×10^{-24}). RNFL thickness was excluded during VIF assessment and was not included in this set.

3.3. Model fitting

3.3.1. 4-Class models

A multivariable ordinal logistic regression model was fitted to the 5 relevant features and patients' age, to determine which variables presented higher regression coefficients. Table 4 summarizes the variables which showed non-zero coefficients, with a significance level of 0.05, for each of the 4-class models. Four features presented coefficients different from zero with a 95% confidence interval, namely RNFL skewness, GCL Gen. Gamma a, GCL thickness, and IPL thickness.

The RNFL skewness presented a positive coefficient, meaning that an increase in one standard deviation on this variable will increase the odds of being in the next severity states of glaucoma by $e^1 = 2.7$ times. For example, when RNFL skewness or RNFL Gen. Gamma a increase by one standard deviation, the odds of being in the categories of Moderate or Severe increase 2.2 times and 1.3 times respectively, when compared with the Healthy and Mild categories. For the GCL and IPL thicknesses, it is the reduction of their value which is associated with an increase in the odds (2.2 times for GCL and 1.5 times for the IPL) of being in a more severe state, because the coefficients are negative.

When fitted to a multivariable linear regression model using the VF MD as the dependent variable, two features presented non-zero coefficients with a 95% confidence level (Table 4). Both features are presented in the previous model (RNFL skewness and IPL thickness). The RNFL skewness is the most significant feature, where an increase of one standard deviation causes a worsening of 3.6 db of the VF MD.

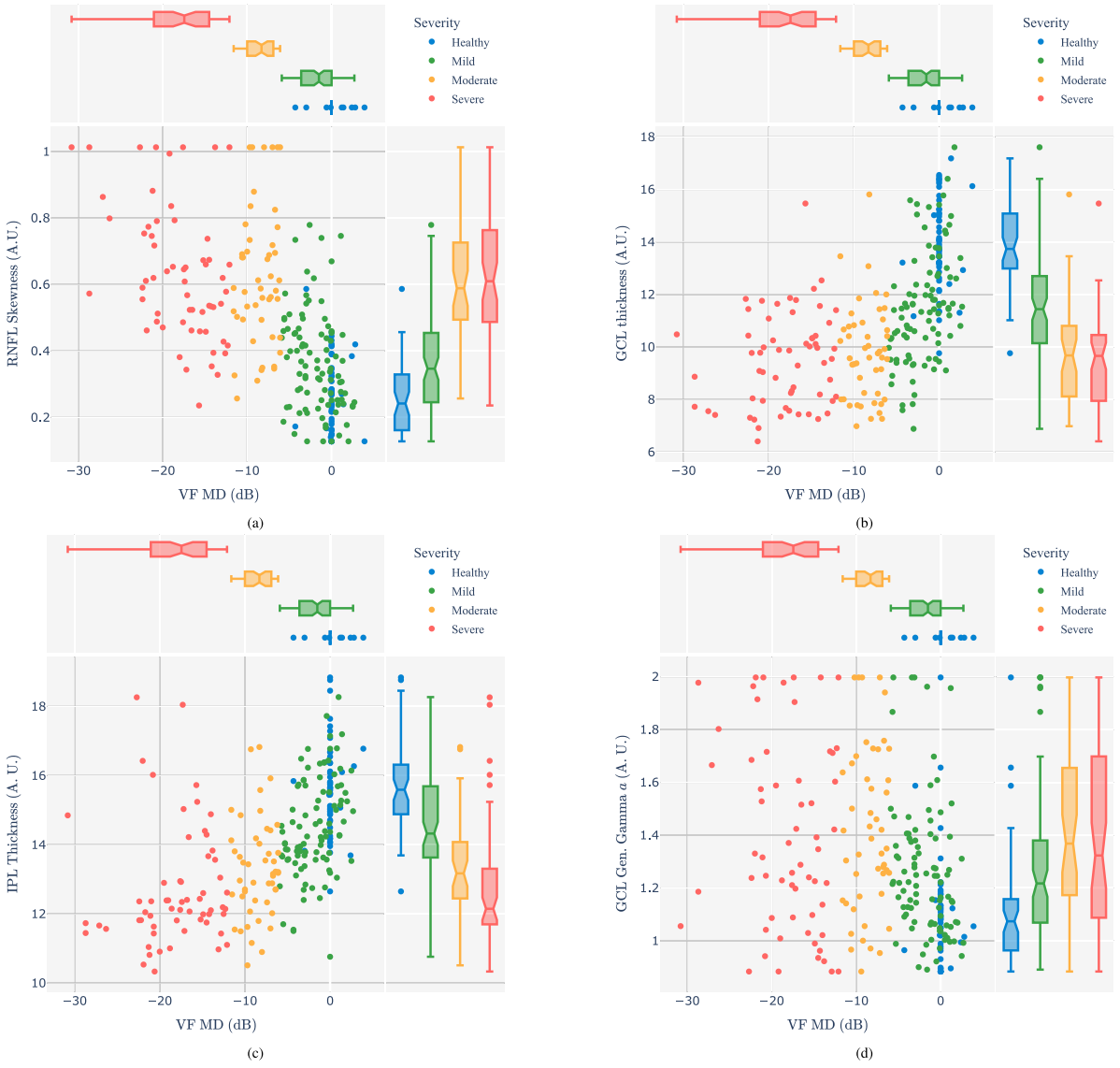

Fig. 3. Four class scatter plot, with marginal box plot of: (a) RNFL skewness vs. VF MD; (b) GCL thickness vs. VF MD; (c) IPL thickness vs. VF MD; (d) GCL Gen. Gamma a vs. VF MD. Healthy subjects without VF MD measurement are represented with VF MD = 0.

The IPL thickness shows positive coefficient, which implies that VF MD worsens (higher glaucoma severity) when this variable decreases.

Fig. 3(a) shows a scatter plot, with marginal box plot, of the distributions of RNFL skewness and VF MD. The data points for the healthy cases are presented for completeness, although the VF MD parameter is only relevant for glaucoma severity. The box plots of the VF MD show, as expected, a perfect separation between the Mild, Moderate and Severe classes. Regarding the RNFL skewness, a clear tendency is shown, confirmed by both the ordinal logistic regression and the linear regression models, passing from lower values to higher ones when the severity of the disease increases. The progression of RNFL skewness is linear, with a gradual increase from Healthy to Mild and then to Moderate/Severe. In the last two stages, the discriminant power of RNFL skewness is reduced.

A lower GCL thickness is visible for Moderate and Severe glaucoma as shown in Fig. 3(b). In addition, GCL thickness in the healthy group stands out from the other categories, as it presents significantly higher thickness (see two-class model Healthy vs. Mild in Section 3.3.2). Among all the tested cases and features, the GCL thickness was the one that achieved the lowest p-value (1.7×10^{-4}). While in both RNFL skewness and GCL thickness the discrimination between Moderate and Severe is difficult, the IPL thickness (Fig. 3(c)) seems to maintain some discrimination power even in advanced stages (see marginal box plot of Fig. 3(c)). Nevertheless, the range of values in the mild group is very extensive, resulting in a lower overall power.

Regarding GCL Gen. Gamma a (Fig. 3(d)), there is an overlapping between the Moderate and Severe groups but a visible variation between the other groups. There is a decreasing tendency when passing from Moderate to Mild and Healthy.

3.3.2. Two-class models

Four different 2-class models were explored in the analysis: Healthy vs. glaucoma, Healthy vs. Mild, Mild vs. Moderate, and Moderate vs. Severe. For each case, a logistic regression model was fitted to the set of 5 relevant variables and patients' age. The significant features for each case are detailed in Table 5.

Table 5
Coefficient values and confidence intervals of statistically significant features for the 2-class fitted models. Statistically significant features implicate a non-zero model coefficient with a confidence level of 95%. AUC stands for the area under the receiver operating characteristic curve.

Logit Regression	Layer	Feature	Coeff.	Conf. Interval 95%	*p*-value	AUC
Healthy vs. Glaucoma	RNFL	Skewness	1.32	[0.20 2.44]	2.1e−02	0.92
	GCL	Thickness	−1.39	[−2.09 – 0.70]	8.7–05	
	GCL	Gen. Gamma *a*	0.73	[0.11 1.36]	2.1e−02	
Healthy vs. Mild	GCL	Thickness	−1.34	[−2.49 – 0.51]	2.8e−03	0.85
	GCL	Gen. Gamma *a*	0.69	[0.07 1.32]	3.0e−02	
Mild vs. Moderate	RNFL	Skewness	1.98	[0.80 3.15]	1.0e−03	0.88
Moderate vs. Severe	–	–	–	–	–	0.65

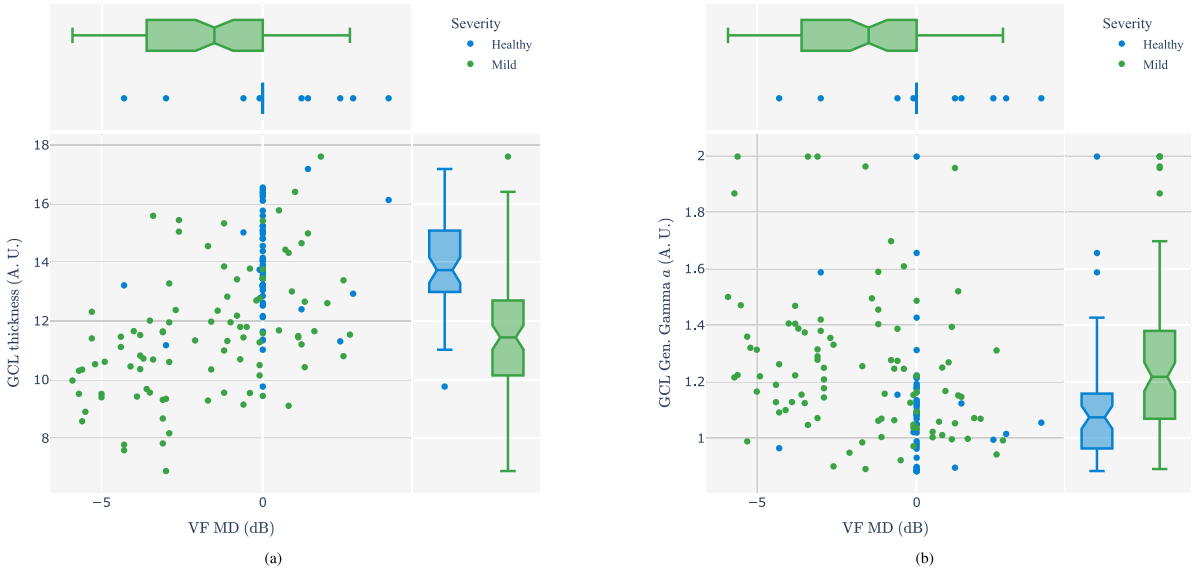

Fig. 4. Two class model, Healthy vs. Mild, scatter plot with marginal box plot of (a) GCL thickness vs. VF MD. (b) GCL Gen. Gamma *a* vs. VF MD. Healthy subjects without VF MD measurement are represented with VF MD = 0.

The first model explores the differences between the healthy individuals and glaucoma patients (Mild, Moderate, and Severe). The logistic regression model showed that the RNFL skewness, GCL thickness, and GCL Gen. Gamma *a* are the features that had a non zero coefficient within a 95% confidence interval. All these features were already relevant in the 4-class models. GCL thickness is the feature with the larger, in terms of absolute value, coefficient (−1.39). Finally, the AUC for this model was computed 0.92.

Regarding the Healthy vs. Mild case, two variables presented a non zero coefficient within a 95% confidence interval, the GCL thickness and the GCL Gen. Gamma *a*. Using the same strategy as before, we can find the odds of having mild glaucoma, compared with healthy subjects, increase 3.8 times when the GCL thickness decreases by one standard deviation and 2 times when the GCL Gen Gamma *a* increases by one standard deviation. Fig. 4(a) shows the scatter plot of GCL thickness and VF MD with marginal box plots. Looking at the scatter distribution, a clear correlation can be seen where lower values of GCL thickness are associated with lower VF MD. Even patients diagnosed with mild glaucoma, but with high VF MD values show a thinner GCL. The distribution of GCL Gen Gamma *a* is shown in Fig. 4(b). This time is the increase of the feature that is correlated with the transition from the Healthy to the Mild group. If we consider this logistic regression model as a linear classifier, it achieves AUC of 0.85.

Regarding the Mild vs. Moderate, one variable presented non zero coefficients with a 95% confidence level, the RNFL skewness. RNFL skewness is the variable with the largest coefficient (1.98). An increase in one standard deviation on this variable will increase the odds of being in the Moderate stage, compared with Mild, by 8 times ($e^{1.98}$ = 7.2). Fig. 5 presents a scatter plot, with marginal box plots, of the RNFL skewness and the VF MD. The distribution is similar to the one found in Fig. 3(a) but, this time, the data is grouped in only two classes, which emphasizes the power of the feature for this specific case.

Lastly, a logistic regression model was also fitted to the Moderate vs. Severe cases. Neither any of the 5 features nor age were able to achieve a coefficient different from 0 with a 95% confidence level.

4. Discussion

The properties of the light scattering in biological tissues have been studied as a diagnostic tool for many diseases (Steelman et al., 2019). The observed patterns allow to infer the density and distribution (spatial arrangement) of the scatterers in a sample, as well as its refractive properties. The high sensitivity of OCT allows to image extremely weak backscattering features in the retina, such as the vitreo-retinal junction, or highly scattering structures, such as the retinal pigment epithelium and the choroid. Therefore, any changes that may happen at the retinal layers as a result of disease, such as glaucoma, may alter the tissue properties and hence, result in changes in the light scattering. The information retrieved from changes in the light scattering can be seen as microstructural biomarkers for the disease diagnosis and staging.

In this work, we used OCT of the macula instead of optic disc OCTs because automatic segmentation of macular OCT is widely available,

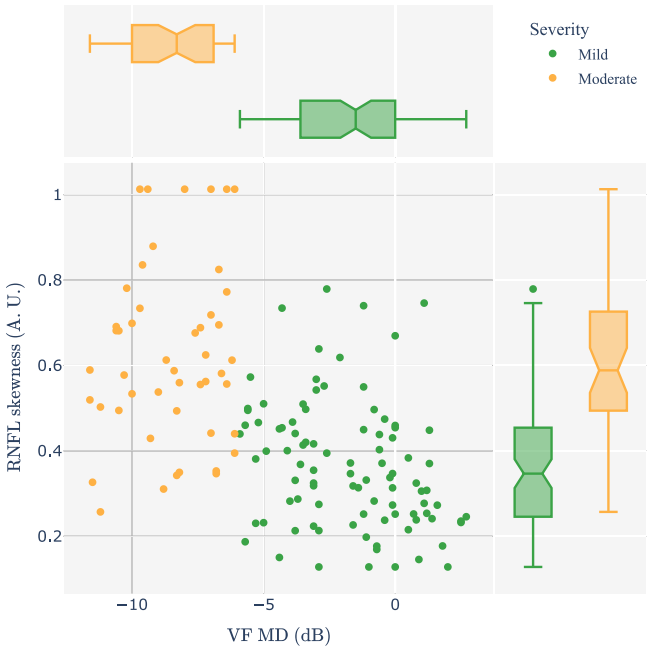

Fig. 5. Two class model, Mild vs. Moderate, scatter plot with marginal box plot of RNFL Skewness vs. VF MD.

with several alternatives obtaining good results while the segmentation of optic disc OCTs is still in extensive development (Marques et al., 2022). Moreover, the effects of glaucomatous damage in the macular region have already been highlighted in several studies, proving that they are also discriminant for the glaucoma diagnosis and staging (Nakatani et al., 2011; Medeiros et al., 2005).

4.1. Statistical analysis

A detailed and comprehensive analysis of a large range of macula-centered OCT speckle features was performed in this study. From the initial set of 470 speckle features (microstruture biomarkers) and 10 anatomical features (macrostructure biomarkers), only 5 features were considered statistically relevant for glaucoma analysis. From these, 4 features (RNFL Skewness, GCL Gen. Gamma a, and thicknesses of GCL and IPL) were considered statistically significant for severity differentiation.

Three features obtained a correlation value with VF MD higher than 0.5, namely the RNFL skewness, GCL thickness, and IPL thickness. The correlation between speckle features and the corresponding thicknesses was also computed as a way to infer both sources of information contain distinct information.

Age, overall, showed a weak negative correlation coefficient with VF MD ($\rho = -0.16$). Nonetheless, this was a significant correlation, which led us to included it as an independent variable in all the models.

4.2. Model fitting

From the subset of 5 features plus age, we identified four that showed statistical significance in logistic and linear regression models. These features can be regarded as possible biomarkers for glaucoma staging. Age was used as a possible biomarker but no significance was found in any of the tested models.

RNFL skewness presented the highest discriminant power over all the tested features. It was the feature with the lowest p-value on the Kruskal–Wallis H test, the one with the highest correlation with VF MD, and it was relevant in the two 4-class models and in two 2-class models. From a physical point of view, skewness is associated with the pixels' intensity distribution along the respective layer. A positive skewness indicates a prevalence of lower intensities (darker pixels) while a negative skewness is evidence of higher intensities (brighter pixels). Brighter pixels on an OCT image are indicative of tissue areas with higher backscattered light, while darker pixels correspond to zones with lower backscattered light (Spicer et al., 2019). From a physiological point of view, lower backscattered signal may be associated to a decrease on the ganglion cell axons as the glaucoma progresses.

The Gen. Gamma a parameter was relevant in the ordinal logistic regression, showing higher values for severe stages of glaucoma than for the early ones. However, its physical interpretation is not straightforward. The Gen. Gamma distribution is a three parameter distribution with applicability in the speckle modeling of tissue with lower scatterer concentrations. The a parameter is the scale parameter of the distribution which controls the maximum values, or the level, of the variable. Thus, a statistically significant variation of this parameter may indicate changes in the light scattered, higher light scattered by the more severe groups of glaucoma, at the region of the GCL.

Speckle-based features present, in general, different information from the thickness features, as shown by their coefficients of correlation with the respective layer thickness (Table 3), which were lower than 0.3 except for GCL Gen. Gamma a. The potential of speckle features proved to be significant, specially for distinguishing Mild vs. Moderate glaucoma where only a speckle feature was statistically significant. This observation indicates that microstructural biomarkers extracted from OCT images are, in fact, related with changes in the microstructure of the tissue and not simply correlated with the macrostructure.

The retinal layers thinning is a known effect of glaucoma (Miki et al., 2014). In our study, the GCL and IPL thicknesses were the ones that showed the best discriminant power for the diagnosis and staging of glaucoma patients. In fact, GCL thinning is known to be an early indicator of glaucoma (Ustaoglu et al., 2019). In our study, it had the highest significance in the Healthy vs. Glaucoma and Healthy vs. Mild regression models. The IPL thickness was relevant in the multivariable linear regression, but with higher p-value than GCL thickness. The RNFL thickness did not appear as a relevant feature in any of the models because it was excluded during the VIF evaluation. Although the RNFL thickness (at the macula) has been reported as a good biomarker for glaucoma diagnosis, it does not have an added value when compared to the parameters presented in the results, *e.g.* the GCL thickness.

The phenomenon called "floor effect" is clearly observable in the results of the Moderate vs. Severe discrimination problem. None of the features, neither thicknesses nor speckle, were significant in this two-class model. Furthermore, this model yielded also the lowest AUC (0.65). The "floor effect" explains how the ability, of OCT imaging technique, to discern further thinning of retinal layers stops before the disease has reached the severe state. Nevertheless, it is interesting to notice that the speckle-based features used in this work were retrieved from a single OCT image and, in the case of RNFL skewness, it is informative enough to observe a significant statistical difference between Mild and Moderate glaucoma subjects.

Neither speckle nor thickness features were significant for the Moderate vs. Severe case. It is possible that other type of damage can still occur in deeper layers, but this information is not collected with current OCTs due to the low signal-to-noise ratio. In order to assess changes in advanced disease stages, other studies (De Jesus et al., 2020) have reported that microvascular density retrieved from OCT angiography (OCTA) is able to discriminate moderate from severe glaucoma, overcoming this limitation of the OCT. This occurs because OCTA is an imaging modality based on temporal speckle variations observed in a sequence of OCT B-scans acquired at the same location.

Traditional OCT imaging was tailored during the last decades to produce the best possible anatomical images, with well defined boundaries and structures. The pre-processing methods applied by device manufacturers change the values of the images within tissue layers to increase the image contrast. The in-built software inevitably changes

the features' statistics, which has major implications on the microstructure biomarkers. Also, OCT volumes are produced averaging several scans with the main purpose to reduce speckle effect. Due to these reasons, the acquisition of un-processed data from OCT devices could still improve the outcome of speckle based biomarkers.

In addition, the OCT image forming process is dependent on the backscattered light, making it very difficult to determine the absorption and scattering coefficients of the studied tissue. Novel ways of assessment of microstructural biomarkers could improve the determination of this type of biomarkers which are correlated with the light properties of the tissue. The general use of other imaging techniques, like spectroscopic optical coherence tomography (Nam and Yoo, 2018), will enable the determination of the tissue wavelength-dependent absorption and scattering coefficients and may lead to more precise determination of these microstructural biomarkers and improve the diagnosis and staging.

Both types of biomarkers, microstructure and macrostructure, have limitations in terms of clinical significance. As discussed before, thickness measurements rapidly suffer from the "floor effect". Moreover, the algorithms used for the thickness determination depend on the device, causing variability in the measurements (Zahavi et al., 2021). Also, the signal-to-noise ratio will certainly decrease with the imaging depth. As a consequence, OCT-based features will be less sensitive to changes that may happen in deeper layers than in upper layers.

This paper focuses on novel imaging features, analyzing their potential in comparison with current state-of-art imaging features, studying their discriminating power and their interpretability. Therefore, the development of an optimal classification model combining all the available information was out of the scope of this paper. Nevertheless, future work on optimization of machine learning models can lead to better results than those presented in this work. Therefore, the data set of 480 features from 258 subjects, as well as code to compute those features in OCT images, was made available as a supplementary material for further investigation (Silva et al., 2023).

As a consequence of the points discussed in this section, some pressing future work directions must be proposed. First, the use of raw, unprocessed, OCT data could improve the sensitivity of microstructure biomakers, specially in advanced stages of glaucoma. Then, the same set of features could be explored in optic disk OCT images. The influence of device variability should also be studied in both speckle and anatomical features. The increment of the data set size could further sustain the conclusions drawn from this work. The use of longitudinal data must also be considered to check the features' ability to detect disease progression in the same subjects. Finally, in view of the recent development of the technique detection-of-apoptosing-retinal-cells (DARC) (Cordeiro et al., 2021), which is able to visualize apoptotic retinal ganglion cells, it would be interesting to correlate speckle features with DARC metrics.

In this work, the layers were analyzed as a single structure. Nevertheless, glaucoma is known to have different effects in different spatial locations (De Jesus et al., 2020). The results could have been understated by considering the layers as a single structure. Then, a sectorial and combined analysis of the OCT volumes of the macular and papilar regions must be performed in future works in order to study the biomarkers in a more precise way. Finally, glaucoma also induces changes in the tissue dynamics, like the retinal blood flow. The exploration of microstructure biomarkers in OCTA data has potential to produce information not captured by standard OCT and surpass the "floor effect" visible in standard OCT features.

5. Conclusion

This work performs, for the first time, a comprehensive and extensive assessment of possible macular OCT speckle biomarkers for the diagnosis and staging of glaucoma. According to our conservative analysis, GCL thickness was confirmed as a good biomarker for glaucoma diagnosis and RNFL skewness is proposed as a good candidate to support the analysis of glaucoma staging. The potential of the analysis of macular OCT speckle features in the context of glaucoma has thus been established.

CRediT authorship contribution statement

Pedro G. Vaz: Conceptualization, Formal analysis, Writing – original draft, Visualization. **Luisa Sanchez Brea:** Conceptualization, Methodology, Formal analysis, Writing – original draft. **Vania Bastos Silva:** Methodology, Software, Writing – original draft. **Jan van Eijgen:** Conceptualization, Validation, Writing – review & editing. **Ingeborg Stalmans:** Validation, Writing – review & editing. **João Cardoso:** Validation, Writing – review & editing, Supervision. **Theo van Walsum:** Validation, Writing – review & editing, Supervision. **Stefan Klein:** Validation, Writing – review & editing, Supervision. **João Barbosa Breda:** Conceptualization, Validation, Writing – review & editing. **Danilo Andrade De Jesus:** Conceptualization, Methodology, Formal analysis, Writing – original draft.

Declaration of competing interest

The authors declare that they have no known competing financial interests or personal relationships that could have appeared to influence the work reported in this paper.

Data availability

The data that has been used is confidential

Acknowledgments

This work was supported by FCT (Fundação para a Ciência e a Tecnologia) under the projects UIDP/04559/2020 and UIDB/04559/2020 to fund Human resources and activities of Laboratory for Instrumentation, Biomedical Engineering and Radiation Physics, and under the project PTDC/EMD-TLM/30295/2017 of European Regional Development Fund (PT-COMPETE 2020). The authors also acknowledge the Laboratory for Advanced Computing at University of Coimbra for providing computing resources that have contributed to the research results reported within this paper (https://www.uc.pt/lca).

Appendix A. Mathematical equations

The main mathematical equations used in this work are depicted in this section.

Rayleigh PDF.

$$p_{RL}(A;a) = \frac{A}{a^2} e^{\left(-\frac{A^2}{2a^2}\right)}, \tag{A.1}$$

where a is the scale parameter.

Gamma PDF.

$$p_G(A;a,d) = \frac{A^{d-1}e^{-A/a}}{a^d \Gamma(d)} \text{ for } a,d>0, \tag{A.2}$$

where d is the shape parameter, a is the scale parameter, and Γ represents the Gamma function (Artin, 2015).

Generalized gamma PDF.

$$p_{GG}(A;a,d,p) = \frac{pA^{d-1}}{a^d \Gamma(d/p)} e^{-(A/a)^p} \text{ for } p>0, \tag{A.3}$$

where d and p are shape parameters, and a, the scale parameter.

K PDF.

$$p_K(A;\upsilon,\varphi,L)=\frac{2\xi^{(\beta+1)/2}A^{(\beta-1)/2}}{\Gamma(L)\Gamma(\varphi)}K_{\varphi-L}(2\sqrt{\xi A})\,, \tag{A.4}$$

where $\beta = L+\varphi-1$, $\xi = L\varphi/\nu$, K_α is a modified Bessel function of the second kind of order α.

Weibull PDF.

$$p_W(A;a,d)=\frac{dA^{d-1}}{a^d}e^{-(A/a)^d}\,, \tag{A.5}$$

where d is shape parameters, and a, the scale parameter.

Nakagami PDF.

$$p_{NK}(A';d,\Omega)=\frac{2d^d}{\Gamma(d)\Omega^d}A'^{2d-1}e^{-\frac{d}{\Omega}A'^2}\,, \tag{A.6}$$

where d is a shape parameter and Ω is a spread parameter.

Rician PDF.

$$p_{RI}(A;a,\nu)=\frac{A}{a^2}e^{-\frac{A^2+\nu^2}{2a^2}}I_0\left(\frac{A\nu}{a^2}\right)\,, \tag{A.7}$$

where ν is the noncentrality parameter and I_0 is the zero order modified Bessel function of the first kind (Abramowitz and Stegun, 1964).

Lognormal PDF.

$$p_L(A;\mu,\sigma)=\frac{1}{\sigma A\sqrt{2\pi}}e^{-\frac{(\log A-\mu)^2}{2\sigma^2}}\,, \tag{A.8}$$

where μ is the mean and σ the standard deviation.

Contrast.

$$C=\frac{\sigma}{\mu}\,, \tag{A.9}$$

where μ is the mean and σ the standard deviation.

SGLDM features.

$$Energy=\sum_{i=0}^{L-1}\sum_{j=0}^{L-1}\sqrt{[s_{\theta,d}(i,j)]^2} \tag{A.10}$$

$$Entropy=\sum_{i=0}^{L-1}\sum_{j=0}^{L-1}-s_{\theta,d}(i,j)\;log\left[s_{\theta,d}(i,j)\right] \tag{A.11}$$

$$Correlation=\frac{\sum_{i=0}^{L-1}\sum_{j=0}^{L-1}(i-\mu_x)(j-\mu_y)s_{\theta,d}(i,j)}{\sigma_x\sigma_y} \tag{A.12}$$

$$Local\ homogeneity=\sum_{i=0}^{L-1}\sum_{j=0}^{L-1}\frac{1}{1+(i-j)^2}s_{\theta,d}(i,j) \tag{A.13}$$

$$Contrast=\sum_{i=0}^{L-1}\sum_{j=0}^{L-1}(i-j)^2s_{\theta,d}(i,j) \tag{A.14}$$

where $s_{\theta,d}(i,j)$ is the (i,j) element of the SGLDM for distance d and direction θ, and,

$$\mu_x=\sum_{i=0}^{L-1}i\sum_{j=0}^{L-1}s_{\theta,d}(i,j) \tag{A.15}$$

$$\mu_y=\sum_{i=0}^{L-1}j\sum_{j=0}^{L-1}s_{\theta,d}(i,j) \tag{A.16}$$

$$\sigma_x=\sum_{i=0}^{L-1}(i-\mu_x)^2\sum_{j=0}^{L-1}s_{\theta,d}(i,j) \tag{A.17}$$

$$\sigma_y=\sum_{i=0}^{L-1}(j-\mu_y)^2\sum_{j=0}^{L-1}s_{\theta,d}(i,j) \tag{A.18}$$

References

Abegão Pinto, L., Willekens, K., Van Keer, K., Shibesh, A., Molenberghs, G., Vandewalle, E., Stalmans, I., 2016. Ocular blood flow in glaucoma–the Leuven eye study. Acta Ophthalmol. 94 (6), 592–598.

Abràmoff, M.D., Garvin, M.K., Sonka, M., 2010. Retinal imaging and image analysis. IEEE Rev. Biomed. Eng. 3, 169–208.

Abramowitz, M., Stegun, I.A., 1964. Handbook of Mathematical Functions with Formulas, Graphs, and Mathematical Tables, Vol. 55. US Government Printing Office, p. 375.

Armstrong, J.J., Wasiuta, T., Kiatos, E., Malvankar-Mehta, M., Hutnik, C.M., 2017. The effects of phacoemulsification on intraocular pressure and topical medication use in patients with glaucoma: a systematic review and meta-analysis of 3-year data. J. Glaucoma 26 (6), 511–522.

Artin, E., 2015. The Gamma Function. Courier Dover Publications.

Bowd, C., Weinreb, R.N., Williams, J.M., Zangwill, L.M., 2000. The retinal nerve fiber layer thickness in ocular hypertensive, normal, and glaucomatous eyes with optical coherence tomography. Arch. Ophthalmol. 118 (1), 22–26.

Bowd, C., Zangwill, L.M., Weinreb, R.N., Medeiros, F.A., Belghith, A., 2017. Estimating optical coherence tomography structural measurement floors to improve detection of progression in advanced glaucoma. Am. J. Ophthalmol. 175, 37–44.

Butt, N.H., Ayub, M.H., Ali, M.H., 2016. Challenges in the management of glaucoma in developing countries. Taiwan J. Ophthalmol. 6 (3), 119–122.

Cordeiro, M.F., Hill, D., Patel, R., Corazza, P., Maddison, J., Younis, S., 2021. Detecting retinal cell stress and apoptosis with DARC: Progression from lab to clinic. Prog. Retinal Eye Res. 100976.

Danielewska, M.E., Antończyk, A., Andrade De Jesus, D., Rogala, M.M., Błońska, A., Ćwirko, M., Kiełbowicz, Z., Iskander, D.R., 2021. Corneal optical coherence tomography speckle in crosslinked and untreated rabbit eyes in response to elevated intraocular pressure. Transl. Vis. Sci. Technol. 10 (5), 2. http://dx.doi.org/10.1167/tvst.10.5.2.

De Jesus, D.A., Brea, L.S., Breda, J.B., Fokkinga, E., Ederveen, V., Borren, N., Bekkers, A., Pircher, M., Stalmans, I., Klein, S., et al., 2020. OCTA multilayer and multisector peripapillary microvascular modeling for diagnosing and staging of glaucoma. Transl. Vis. Sci. Technol. 9 (2), 58.

De Pretto, L.R., Nogueira, G.E., Freitas, A.Z., 2015. New speckle analysis method for optical coherence tomography signal based on autocorrelation. In: Biophotonics South America, Vol. 9531. SPIE, pp. 456–464.

Demidov, V., Matveev, L.A., Demidova, O., Matveyev, A.L., Zaitsev, V.Y., Flueraru, C., Vitkin, I.A., 2019. Analysis of low-scattering regions in optical coherence tomography: applications to neurography and lymphangiography. Biomed. Opt. Express 10 (8), 4207–4219.

Gary, R.G., Rolland, J.P., Parker, K.J., 2021. Speckle statistics of biological tissues in optical coherence tomography. Biomed. Opt. Express 12 (7), 4179–4191.

Ghosh, D., Vogt, A., 2012. Outliers: An evaluation of methodologies. In: Joint Statistical Meetings, Vol. 2012.

Gmeiner, J.M., Schrems, W.A., Mardin, C.Y., Laemmer, R., Kruse, F.E., Schrems-Hoesl, L.M., 2016. Comparison of bruch's membrane opening minimum rim width and peripapillary retinal nerve fiber layer thickness in early glaucoma assessment. Invest. Ophthalmol. Vis. Sci. 57 (9), OCT575–OCT584.

Guedes, G., C. Tsai, J., A. Loewen, N., 2011. Glaucoma and aging. Curr. Aging Sci. 4 (2), 110–117.

Hilal, M., Gaudêncio, A.S., Vaz, P.G., Cardoso, J., Humeau-Heurtier, A., 2022. Colored texture analysis fuzzy entropy methods with a dermoscopic application. Entropy 24 (6), 831.

Iskander, D.R., Kostyszak, M.A., Jesus, D.A., Majewska, M., Danielewska, M.E., Krzyzanowska-Berkowska, P., 2020. Assessing corneal speckle in optical coherence tomography: a new look at glaucomatous eyes. Optom. Vis. Sci. 97 (2), 62–67.

Jesus, D.A., Barbosa Breda, J., Van Keer, K., Rocha Sousa, A., Abegão Pinto, L., Stalmans, I., 2019. Quantitative automated circumpapillary microvascular density measurements: a new angioOCT-based methodology. Eye 33 (2), 320–326.

Jesus, D.A., Iskander, D.R., 2015. Age-related changes of the corneal speckle by optical coherence tomography. In: 2015 37th Annual International Conference of the IEEE Engineering in Medicine and Biology Society. EMBC, IEEE, pp. 5659–5662.

Jesus, D.A., Iskander, D.R., 2017. Assessment of corneal properties based on statistical modeling of OCT speckle. Biomed. Opt. Express 8 (1), 162–176.

Jesus, D.A., Majewska, M., Krzyżanowska-Berkowska, P., Iskander, D.R., 2017. Influence of eye biometrics and corneal micro-structure on noncontact tonometry. PLoS One 12 (5), e0177180.

Kasaragod, D.K., Lu, Z., Smith, L.E., Matcher, S.J., 2010. Speckle texture analysis of optical coherence tomography images. In: Speckle 2010: Optical Metrology, Vol. 7387. SPIE, pp. 553–559.

Kim, J.H., 2019. Multicollinearity and misleading statistical results. Korean J. Anesthesiol. 72 (6), 558–569.

Kirillin, M.Y., Farhat, G., Sergeeva, E.A., Kolios, M.C., Vitkin, A., 2014. Speckle statistics in OCT images: Monte Carlo simulations and experimental studies. Opt. Lett. 39 (12), 3472–3475.

Kostianeva-Zhelinska, S.S., Konareva-Kostianeva, M., Atanassov, M., 2018. Optical coherence tomography parameters in preperimetric open-angle glaucoma. Open J. Ophthalmol. 8 (2), 106–119.

Kuang, T.M., Zhang, C., Zangwill, L.M., Weinreb, R.N., Medeiros, F.A., 2015. Estimating lead time gained by optical coherence tomography in detecting glaucoma before development of visual field defects. Ophthalmology 122 (10), 2002–2009.

Marques, R., De Jesus, D.A., Breda, J., Van Eijgen, J., Stalmans, I., van Walsum, T., Klein, S., Vaz, P.G., Brea, L.S., 2022. Automatic segmentation of the optic nerve head region in optical coherence tomography: A methodological review. Comput. Methods Programs Biomed. 106801.

Medeiros, F.A., Zangwill, L.M., Bowd, C., Vessani, R.M., Susanna, Jr., R., Weinreb, R.N., 2005. Evaluation of retinal nerve fiber layer, optic nerve head, and macular thickness measurements for glaucoma detection using optical coherence tomography. Am. J. Ophthalmol. 139 (1), 44–55.

Miki, A., Medeiros, F.A., Weinreb, R.N., Jain, S., He, F., Sharpsten, L., Khachatryan, N., Hammel, N., Liebmann, J.M., Girkin, C.A., et al., 2014. Rates of retinal nerve fiber layer thinning in glaucoma suspect eyes. Ophthalmology 121 (7), 1350–1358.

Mohammadzadeh, V., Fatehi, N., Yarmohammadi, A., Lee, J.W., Sharifipour, F., Daneshvar, R., Caprioli, J., Nouri-Mahdavi, K., 2020. Macular imaging with optical coherence tomography in glaucoma. Surv. Ophthalmol. 65 (6), 597–638.

Nakatani, Y., Higashide, T., Ohkubo, S., Takeda, H., Sugiyama, K., 2011. Evaluation of macular thickness and peripapillary retinal nerve fiber layer thickness for detection of early glaucoma using spectral domain optical coherence tomography. J. Glaucoma 20 (4), 252–259.

Nam, H.S., Yoo, H., 2018. Spectroscopic optical coherence tomography: a review of concepts and biomedical applications. Appl. Spectrosc. Rev. 53 (2–4), 91–111.

Niemczyk, M., Danielewska, M.E., Kostyszak, M.A., Lewandowski, D., Iskander, D.R., 2021. The effect of intraocular pressure elevation and related ocular biometry changes on corneal OCT speckle distribution in porcine eyes. PLoS One 16 (3), e0249213.

Patel, D.E., Cumberland, P.M., Walters, B.C., Russell-Eggitt, I., Rahi, J.S., Group, O.S., 2015. Study of optimal perimetric testing in children (OPTIC): feasibility, reliability and repeatability of perimetry in children. PLoS One 10 (6), e0130895.

Ranganathan, P., Pramesh, C., Aggarwal, R., 2017. Common pitfalls in statistical analysis: Logistic regression. Pers. Clin. Res. 8 (3), 148.

Repository, 2023. Speckle OCT repository. Python code available at https://gitlab.com/l3151/speckle-oct-les.

Roy, A.G., Conjeti, S., Carlier, S.G., König, A., Kastrati, A., Dutta, P.K., Laine, A.F., Navab, N., Sheet, D., Katouzian, A., 2015. Bag of forests for modelling of tissue energy interaction in optical coherence tomography for atherosclerotic plaque susceptibility assessment. In: 2015 IEEE 12th International Symposium on Biomedical Imaging. ISBI, IEEE, pp. 428–431.

Silva, V., Brea, L., Jesus, D., Vaz, P., 2023. LES speckle OCT repository. URL: https://gitlab.com/l3151/speckle-oct-les.

Silva, V.B., De Jesus, D.A., Klein, S., van Walsum, T., Cardoso, J., Brea, L.S., Vaz, P.G., 2022. Signal-carrying speckle in optical coherence tomography: a methodological review on biomedical applications. J. Biomed. Opt. 27 (3), 030901.

Society, E.G., 2021. Terminology and guidelines for glaucoma, 5th edition. Br. J. Ophthalmol. 105 (Suppl 1), 1–169. http://dx.doi.org/10.1136/bjophthalmol-2021-egsguidelines.

Spicer, G., Eid, A., Wangpraseurt, D., Swain, T.D., Winkelmann, J., Yi, J., Kuhl, M., Marcelino, L., Backman, V., 2019. Measuring light scattering and absorption in corals with inverse spectroscopic optical coherence tomography (ISOCT): a new tool for non-invasive monitoring. Sci. Rep. 9 (1), 1–12.

Steelman, Z.A., Ho, D.S., Chu, K.K., Wax, A., 2019. Light-scattering methods for tissue diagnosis. Optica 6 (4), 479–489.

Tham, Y.-C., Li, X., Wong, T.Y., Quigley, H.A., Aung, T., Cheng, C.-Y., 2014. Global prevalence of glaucoma and projections of glaucoma burden through 2040: a systematic review and meta-analysis. Ophthalmology 121 (11), 2081–2090.

Ustaoglu, M., Solmaz, N., Onder, F., 2019. Discriminating performance of macular ganglion cell-inner plexiform layer thicknesses at different stages of glaucoma. Int. J. Ophthalmol. 12 (3), 464.

Vaz, P.G., Humeau-Heurtier, A., Figueiras, E., Correia, C., Cardoso, J., 2016. Laser speckle imaging to monitor microvascular blood flow: a review. IEEE Rev. Biomed. Eng. 9, 106–120.

Vaz, P.G., Humeau-Heurtier, A., Figueiras, E., Correia, C., Cardoso, J., 2017. Effect of static scatterers in laser speckle contrast imaging: an experimental study on correlation and contrast. Phys. Med. Biol. 63 (1), 015024.

Weinreb, R.N., Aung, T., Medeiros, F.A., 2014. The pathophysiology and treatment of glaucoma: a review. JAMA 311 (18), 1901–1911.

Wu, Y., Szymanska, M., Hu, Y., Fazal, M.I., Jiang, N., Yetisen, A.K., Cordeiro, M.F., 2022. Measures of disease activity in glaucoma. Biosens. Bioelectron. 196, 113700. http://dx.doi.org/10.1016/j.bios.2021.113700, URL: https://www.sciencedirect.com/science/article/pii/S0956566321007375.

Zahavi, O., Domínguez-Vicent, A., Brautaset, R., Venkataraman, A.P., 2021. Evaluation of automated segmentation algorithm for macular volumetric measurements of eight individual retinal layer thickness. Appl. Sci. 11 (3), 1250.